Chemical Science

ROYAL SOCIETY OF CHEMISTRY

EDGE ARTICLE

View Article Online
View Journal | View Issue

Check for updates

Cite this: *Chem. Sci.*, 2024, **15**, 618

All publication charges for this article have been paid for by the Royal Society of Chemistry

Received 3rd October 2023
Accepted 27th November 2023

DOI: 10.1039/d3sc05212e

rsc.li/chemical-science

Selective chiral dimerization and folding driven by arene–perfluoroarene force†

Qiuhong Cheng, Aiyou Hao * and Pengyao Xing *

Oligomerization and folding of chiral compounds afford diversified chiral molecular architectures with interesting chiroptical properties, but their rational and precise control remain poorly understood. In this work, we employed arene–perfluoroarene (AP) interaction to manipulate the folding and dimerization of alanine derivatives bearing pyrene and a perfluoronaphthalene derivative. Based on X-ray crystallography and nuclear magnetic resonance, the compound with a smaller tether and high skeleton rigidity self-assembled into double helical dimers by duplex hydrogen bonding and AP forces in a less polar solvent. Reversible disassociation occurred upon switching to a dipolar solvent or applying heating–cooling cycles. In comparison, the compound with increased skeleton flexibility folds into chiral molecular clamps in a less polar solvent, and is transformed into planar dimers upon switching to a polar solvent. The dynamic geometrical transformation between dimerization and folding was accompanied by chiroptical switching. Beyond the molecular and supramolecular level, we showed hierarchy control in the self-assembled nanoarchitectures and columnar and lamellar arrangements of their molecular packing. This work utilized AP forces to prepare and manipulate the chiral architectures at different hierarchical levels, enriching methodologies in precise chiral synthetic chemistry.

Introduction

Supramolecular self-assembly from chiral units widely occurs in natural products.[1,2] Point chirality in amino acids or nucleic acid transfer on the supramolecular or macroscopic scale through noncovalent force-driven self-assembly provide functions of bio-information storage and selective chiral recognition.[3–8] In addition to self-assembly, intrinsic folding by noncovalent forces also creates complicated helical structures, such as the secondary structures of peptides, proteins and polysaccharides.[9–13] The preference towards chiral folding and self-assembly dramatically influences the resulting structure and functions, while the structural basis still remains a mystery.[14,15] For simpler synthetic chiral building units, rational control of the balance between intramolecular folding and intermolecular oligomerization is crucial for the precise synthesis of chiral self-assembled materials.[16]

Small chiral compounds bearing two or multiple aromatic entities are effective building units in constructing functional soft materials, which is ascribed to the directional growth aided by diverse aromatic forces.[17–21] Peptides from aromatic amino acids, and N-terminal aryl peptides and amino acids fall into this scope.[22–25] Their potentials in self-assembly have been intensively explored, while the intramolecular folding by π-forces between aryl segments is rarely referred to ref. 26–28. Identification of the folding behaviors and their structural basis facilitates the manipulation and fabrication of novel functional chiral materials for asymmetric catalysis, recognition and sensing applications. For example, recently, Alcázar and our group unveiled folded molecular tweezers in ditryptophan peptide derivatives and explored their functions in the recognition of electron-deficient guests and chiroptical properties.[29,30] Possible interactions between aryl entities include π–π stacking (ionic-π and cation-π), charge-transfer interaction and arene–perfluoroarene (AP) interaction.[22,24,31–33] AP interaction occurs between planar fused aromatic rings and perfluorinated aromatic compounds.[34] Fluorination produces an inverted electron distribution compared to hydrocarbons, so that perfluoroarene with π-holes would generate multiple F⋯H hydrogen bonds and π⋯π-hole interactions. Thus, the AP interaction has stronger binding affinity than the π–π interaction.[35] For example, in the gas phase, the binding energy of benzene–hexafluorobenzene is about twice as high as that of benzene–benzene complexes.[36] AP interaction has been used in tuning supramolecular chirality, structure and properties in multiple constituent systems, yet its application in tuning folding and self-assembly behaviors has not been reported so far.[37,38]

In this work, naphthalene-F_7 was conjugated to pyrene appended alanine. The resulted building units, namely PMA (*N*-

---

Key Laboratory of Colloid and Interface Chemistry of Ministry of Education, School of Chemistry and Chemical Engineering, Shandong University, Jinan 250100, People's Republic of China. E-mail: haoay@sdu.edu.cn; xingpengyao@sdu.edu.cn

† Electronic supplementary information (ESI) available. CCDC 2246067, 2246071, 2246072 and 2246095. For ESI and crystallographic data in CIF or other electronic format see DOI: https://doi.org/10.1039/d3sc05212e

(1-oxo-1-((3-((perfluoronaphthalen-2-yl)amino)propyl)amino)propan-2-yl)pyrene-1-carboxamide) and PBA (*N*-(1-oxo-1-((3-((perfluoronaphthalen-2-yl)amino)propyl)amino)propan-2-yl)-4-(pyren-1-yl)butanamide), bear both the AP donor and an acceptor with either a rigid or flexible tether. In the solid state, X-ray crystallography indicates that ^{L}**PMA** and ^{L}**PBA** adopt a double helical dimer and planar dimer structure, respectively. In contrast, $^{D/L}$PMA in the racemic state afforded a planar dimer, while $^{D/L}$PBA folded into chiral foldamers. In the homochiral and heterochiral modality, AP interaction and hydrogen bonds are dominating. In the solution phase, solvent polarity varied the preference towards folding and oligomerization. In dimethyl sulfoxide (DMSO), PMA remains in a monomer state, and in less polar chloroform ($CHCl_3$), dimers are generated, and the monomer–dimer transformation is reversibly controlled by a heating–cooling process. In contrast, PBA with a flexible tether forms a dimer in $CHCl_3$, and folds in dipolar solvent DMSO. Further heating of the DMSO solution would break down the AP and hydrogen bonds into a monomeric state. Finally, we explored the self-assembly into nanoarchitectures, where double helical and planar dimers of ^{L}**PMA** and ^{L}**PBA** packed into columnar and lamellar structures, respectively, showed a hierarchical impact from molecular to supramolecular to nanoscale. This work introduces an AP interaction to manipulate folding and hierarchical self-assembly with controlled supramolecular chirality that may enrich the rational and precise synthesis of chiral functional materials (Scheme 1).

Results and discussion

The synthesis of PMA and PBA was through several steps including aromatic substitution and amide condensation reactions (Schemes S1 and S2†). ^{1}H, ^{13}C and ^{19}F nuclear magnetic resonance (NMR) and mass spectra were used to fully characterize the enantiomerically pure compounds (Fig. S1–S24†). Most AP complexation was realized in perfluorinated compounds such as naphthalene-F_8, as the substitution by electron-rich nitrogen would degenerate the electron density of π-holes and the corresponding AP forces.[36] In order to probe the occurrence of AP-initiated self-assembly, single crystals were carefully cultivated *via* solvent evaporation and the corresponding enantiopure X-ray structures are shown in Fig. 1 (Tables S1–S4†). ^{L}**PMA** with a rigid skeleton features a dimeric geometry (Fig. 1a), where pyrene and naphthalene-F_7 segments are closely packed in a head-to-tail manner. Two PMA molecules are packed into a double helical screw sense driven structure and stabilized by multiple noncovalent forces. Between the amide groups, two hydrogen bonds are formed, and the nearly parallel (d = 3.43 Å) pyrene/naphthalene-F_7 arrays imply the occurrence of the AP force. Non-covalent interaction (NCI)/reduced density gradient (RDG) analysis on the dimers suggests the presence of aromatic forces between the pyrene and naphthalene-F_7 moieties (green regions in Fig. 1b) as well as H-bond interaction (blue regions in Fig. 1b and S25†).[39,40] Hirshfeld surfaces (bottom of Fig. 1b) also confirmed the crucial role of hydrogen bonds and AP forces in dimerization.[41] Decomposed intermolecular contact distributions based on the Hirshfeld surfaces of the dimers are highlighted on the fingerprint graphics (Fig. 1c). F⋯H occupied the largest fraction of up to 35.4%. Other related forces including C⋯C and F⋯C show fractions of 12.1% and 7.5%, respectively. In contrast, O⋯H only shows a fraction of 8.5%. Due to AP interaction primarily consisting of F⋯H and π⋯π-hole interactions, the above results suggest that AP forces mainly drive the dimerization, and are also aided by hydrogen bonds (Fig. S26†). In comparison, PBA possesses an elongated alkyl spacer with enhanced structural flexibility. A dimeric structure was found in ^{L}**PBA** as well (Fig. 1d). ^{L}**PBA** adopts a face-to-face dimer orientation supported by duplex hydrogen bonds and AP interaction (d = 3.51 Å). NCI analysis suggests the crucial role of hydrogen bonds and AP forces as well (Fig. 1e). The calculated fingerprint diagram shows an F⋯H fraction of 22.2%, lower than that of ^{L}**PMA** (35.4%). Also, the fraction of C⋯C (8%, assigned as the π⋯π hole short contacts) is lower than that of ^{L}**PMA** (12.1%) (Fig. S27†). The contribution of AP forces in the dimerization is reduced, along with increased spacer length and structural flexibility.

Wallach's rule tells us that the single crystal of a racemic mixture is always denser than that of its enantiomers.[42,43] In addition to Wallach's rule, we speculated that, in the racemic form, an alternative self-assembly modality might be adopted. Single crystals of the racemic mixtures were cultivated, as shown in Fig. 2. $^{D/L}$PMA surprisingly afforded a dimeric structure, consistent with its enantiomeric counterparts. Duplex hydrogen bonds and AP interactions are present as well. NCI analysis of the $^{D/L}$PMA dimer and ^{L}**PBA** folder also suggest the presence of AP and hydrogen bond interactions (Fig. S28 and S29†). However, we noticed that the overlapping of pyrene/naphthalene-F_7 regions is deficient compared to ^{L}**PMA**. The F⋯H fraction (27.7%) is significantly lower than ^{L}**PMA** (35.4%) (Fig. S30†). Instead of screw sense, face-to-face dimerization emerged. Our intuitive understanding is that $^{D/L}$PMA dimerization is less energetically favored, in contrast to the enantiopure form. Based on the X-ray structures, the dimerization interaction energies were calculated at the theory level of b3lyp/def2SVP-D3(BJ) (left diagram of Fig. 2c). In the enantiopure form, the mean dimerization energy is determined as -35.3 kcal mol^{-1}. This value is much higher than that for most noncovalent forces such as hydrogen bonds and π–π stacking, due to the presence of multiple interactions. In the racemic form, the dimerization binding energy is 27.0 kcal mol^{-1}, much lower than that of the enantiopure state, which is in good agreement with the X-ray structure analysis and assumptions. Wallach's rule emphasizes the high space utilization in the racemic form, yet in the present case, the binding affinity is lower than for the enantiopure counterpart. Nevertheless, chiral self-resolution was not observed in the crystallization of PMA racemates.

Next, the self-assembly of PBA in the racemic form was probed using X-ray crystal structures. Surprisingly, $^{D/L}$PBA does not show dimers. Instead, intramolecular folding occurs (Fig. 2b). ^{D}PMA and ^{L}**PMA** individually folded into enantioselective mirror conformations. Folding is facilitated by the

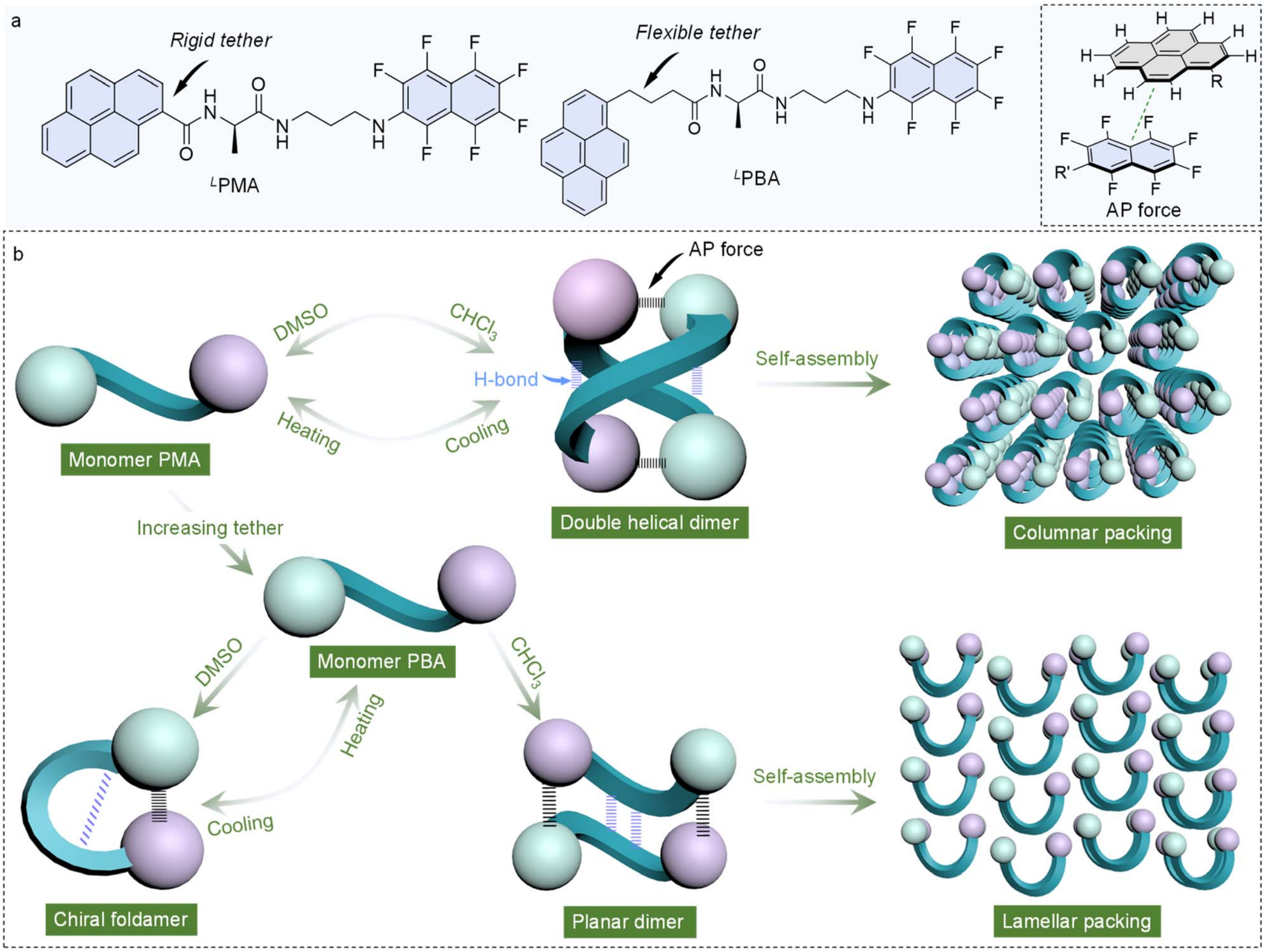

Scheme 1 (a) Molecular structure of building units and the presentation of the AP force; (b) structural evolution of the two building units controlled by tether flexibility, solvent and heating/cooling process.

hydrogen bonds and AP interaction. For PBA, hydrogen bonding occurred between the amine NH adjacent to the naphthalene-F_7 and amide C═O. The intramolecular folding allows for sufficient overlap between pyrene and naphthalene-F_7, which gives rise to a high F⋯H fraction (30.6%) (Fig. S31†). This implies that PBA, compared to PMA, has the potential to form folded structures, which might be due to the low binding affinity to afford heterochiral dimers or other self-assemblies, while the flexibility of alkyl chains conformationally favors the folding topology. The energy landscapes give insights into the pathway complexity (Fig. 2c). PMA folding shows lower interaction energy (22.4 kcal mol^{-1}) compared to that of PBA (25.9 kcal mol^{-1}), and the energy gaps (Δ) between homochiral dimerization and the folding of PMA and PBA are 12.9 kcal mol^{-1} and 5.6 kcal mol^{-1}, respectively. The small Δ value of PBA between dimerization and folding implies that, in the enantiopure form, PBA may realize transformation between the two states, while the transformation for PMA is energetically unfavorable.

To further demonstrate the importance of AP interaction in forming a folded structure, DFT-based computational studies were employed. A model compound was constructed without AP interaction through modifying the single crystal structure of the PBA dimer. We replaced naphthalene-F_7 with a methyl group to eliminate AP interaction (Fig. S32†). After structural optimization, more hydrogen bonds appear and the methyl group is away from the pyrene ring, indicating that the molecule does not prefer to form a folded structure without AP interaction. As shown in Fig. S33a,† the main hydrogen bond to drive the folding is N1–H⋯O1. To completely avoid the influence of hydrogen bonding, N1 and N2 were both replaced with O (Fig. S33c and d†). After optimization, no hydrogen bond was found, while a folded structure was retained, driven by AP interaction. This suggests the vital role of AP interaction in driving the formation of the folder (Fig. S33e and S34†). Molecular dynamics (MD) simulation was also used to monitor the transformation process from a non-folding to a folding conformation of a model molecule. A non-folding conformation was used as the initial structure and placed in a box with a volume of $5 \times 5 \times 5$ nm^3 to observe the conformation transition over time. The MD simulation was conducted using the GROMACS 2020 program, with a total simulation time of 30 ns. As shown in Fig. S35,† the simulation system reached equilibrium in less than 1 ns. The molecular structure changes

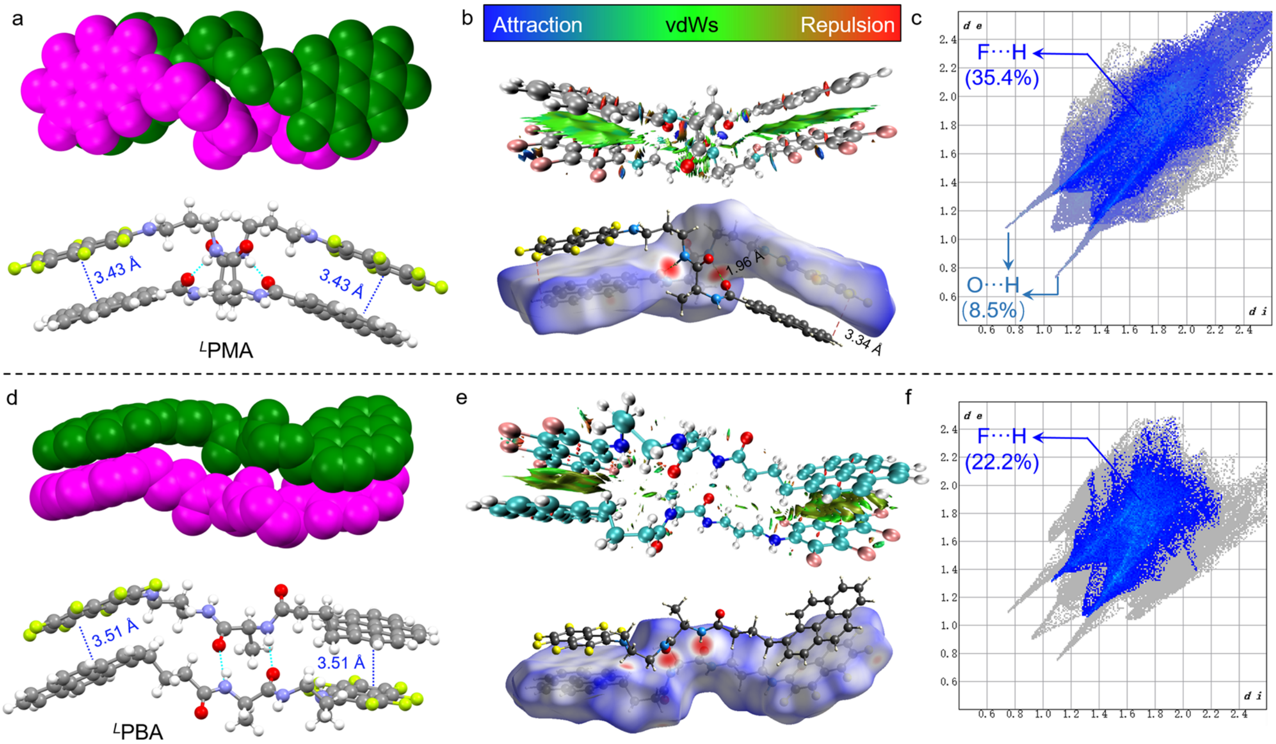

Fig. 1 (a) X-ray structures of ^{L}PMA dimers. (b) Noncovalent interaction analysis of ^{L}PMA dimers. The green regions represent vdWs interactions. (c) Short contact fraction distributions in ^{L}PMA dimers. (d–f) X-ray structures and the corresponding noncovalent interaction analysis of ^{L}PBA dimers.

dramatically in the early stage of the simulation. After reaching equilibrium, the molecule existed in a folded conformation induced by the AP interaction. The distance between C1 and C2 obviously decreased and eventually stabilized around 4 Å, demonstrating the conformation transformation from a non-folded to a folded state. Moreover, hydrogen bonds were not observed in this simulation system.

Noncovalent forces including AP and hydrogen bonds are sensitive to solvent environments. Protic or polar solvents such as DMSO would normally destroy noncovalent forces *via* solvation, while less polar solvents such as $CHCl_3$, dichloroethane (DCE) or methyl cyclohexane (MCH) may prefer the occurrence of noncovalent forces. Additionally, the volume ratio between DMSO and $CHCl_3$ was altered to probe the structural evolution in solution. With increasing volume fraction of DMSO (f_{DMSO}) against $CHCl_3$, absorbance at around 350 nm was enhanced with slight hypochromic shifts (Fig. 3a). This change is reminiscent of the disassociation of self-assemblies driven by aromatic stacking forces. The disassembly process of PMA and PBA leads to the variations in the fluorescence.[44–46] For PMA, the emission intensity was enhanced initially, and then declined in high f_{DMSO} regions (Fig. 3a). The major emission peak at 407 nm hypsochromically shifted to 402 nm once DMSO was added, which is in accordance with the disappearance of AP interaction. **^{L}PBA** shares a similar structure with **^{L}PMA**, while with increasing f_{DMSO}, the absorbance decreased slightly, in sharp contrast to **^{L}PMA** (Fig. 3b). The emission intensity at around 400 nm decreased with increasing intensity at a bathochromic-shifted wavelength of around 500 nm. The spectroscopic changes with increasing f_{DMSO} suggest structural evolution beyond the disassociation. We speculated that first, DMSO destroys the hydrogen bonds leading to the disassembly of the PBA dimer. Then, due to the flexible tether of PBA compared with PMA, AP interaction drives the formation of a foldamer. Further heating of the DMSO solution would destroy hydrogen bonds and intramolecular AP interaction to afford monomers. AP complexation lowers the energy gap of frontier orbitals. For example, **^{L}PBA** in the free monomer state gives a gap of 3.91 eV between the lowest unoccupied molecular orbital (LUMO) and the highest occupied molecular orbital (HOMO), while this is slightly reduced to 3.78 eV after AP-driven folding. Due to the more sufficient AP overlap in foldamers (F⋯H fraction: 30.6%) than dimers (F⋯H fraction: 22.2%), more bathochromic shifts would be generated. This thus supports the assumption that self-assemblies and folded structures are formed in $CHCl_3$ and DMSO, respectively. Temperature-variable emission spectroscopy was performed using high boiling point DCE to replace $CHCl_3$ (Fig. 3c–e). Upon heating **^{L}PMA** from 293 to 343 K, **^{L}PMA** shows a decreased emission intensity ascribed to the disassociation of self-assemblies with enhanced molecular motion, and the subsequent cooling results in full recovery to the initial intensity (Fig. 3e). However, the emission intensity of **^{L}PBA** was slightly enhanced (Fig. 3d) upon heating, and upon subsequent cooling it could hardly be recovered. This difference verifies that **^{L}PMA** may adopt an assembly/disassociation cycle while **^{L}PBA** is under structural transformation from dimerization to folding in

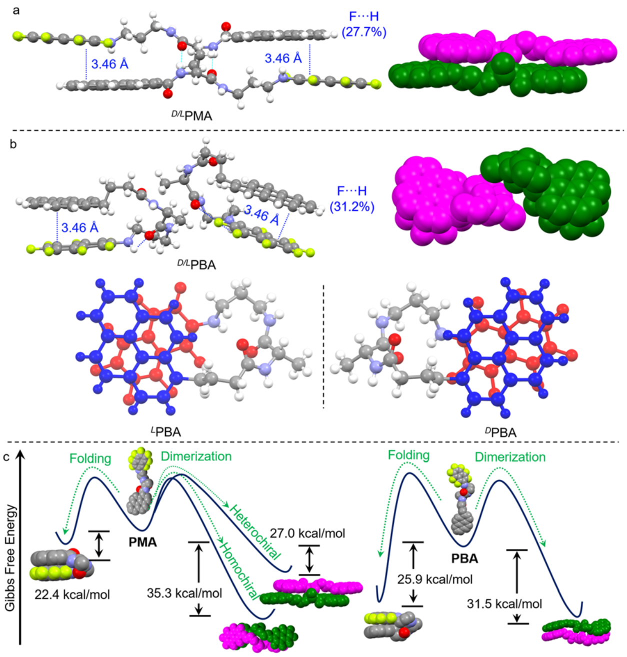

Fig. 2 (a) X-ray structures of $^{D/L}$PMA. (b) X-ray structures of $^{D/L}$PBA, and an illustration of the folded enantiomers. (c) Energy landscape of the self-assemblies in the homochiral and heterochiral complexation (left: PMA, right: PBA).

the heating–cooling process. In the subsequent cooling, foldamer formation resulted in hysteresis that delays the emission recovery.

To correlate the spectral variations in the solutions, we performed ^{1}H NMR spectroscopy in CDCl$_3$ and DMSO-d_6. Concentration dependent ^{1}H NMR spectra from 0.05 mM to 2.0 mM in CDCl$_3$ were collected (Fig. 4a, b, S36 and S37†). The active protons of Ha, Hb and Hc are located between 5.0 and 7.0 ppm. With increasing concentration, amide protons Ha and Hb shifted to lower fields, with self-assembly contributing to the shift. Based on the X-ray structures (Fig. 1), the dimerization involves the amide complementary hydrogen bonds, while Hc does not participate. Thus, in the low polarity CDCl$_3$, dimerization is expected. In contrast, concentration-dependent ^{1}H NMR spectra in DMSO-d_6 showed no apparent shifts, supporting the absence of self-assembly (Fig. S38 and S39†). Partial ^{1}H NMR spectra of Hc (Fig. S40†) indicate the different locations of Hc. Hc of **^{L}PMA** and Hc of **^{L}PBA** are located at 6.13 and 6.30 ppm, respectively, while in CDCl$_3$ they share an identical location (Fig. 4b). This phenomenon suggests that Hc is in different chemical environments for **^{L}PMA** and **^{L}PBA**. Also, we observed that when increasing the concentration from 0.1 to 10 mM in DMSO-d_6, Hc of **^{L}PBA** shows larger shifts to higher fields, which may be caused by the intramolecular folding. Based on the X-ray structure, Hc is involved in hydrogen bonds in the **^{L}PBA** foldamers (Fig. S41 and S42†). Then, temperature-variable ^{1}H NMR spectroscopy was performed (Fig. 4c, S43 and S44†). From 298 K to 343 K, the aromatic protons of **^{L}PBA** are barely shifted, indicating that the conformations are retained. In comparison, the aromatic protons (pyrene domain) of **^{L}PMA** shift to lower fields upon heating. Meanwhile, Hf and

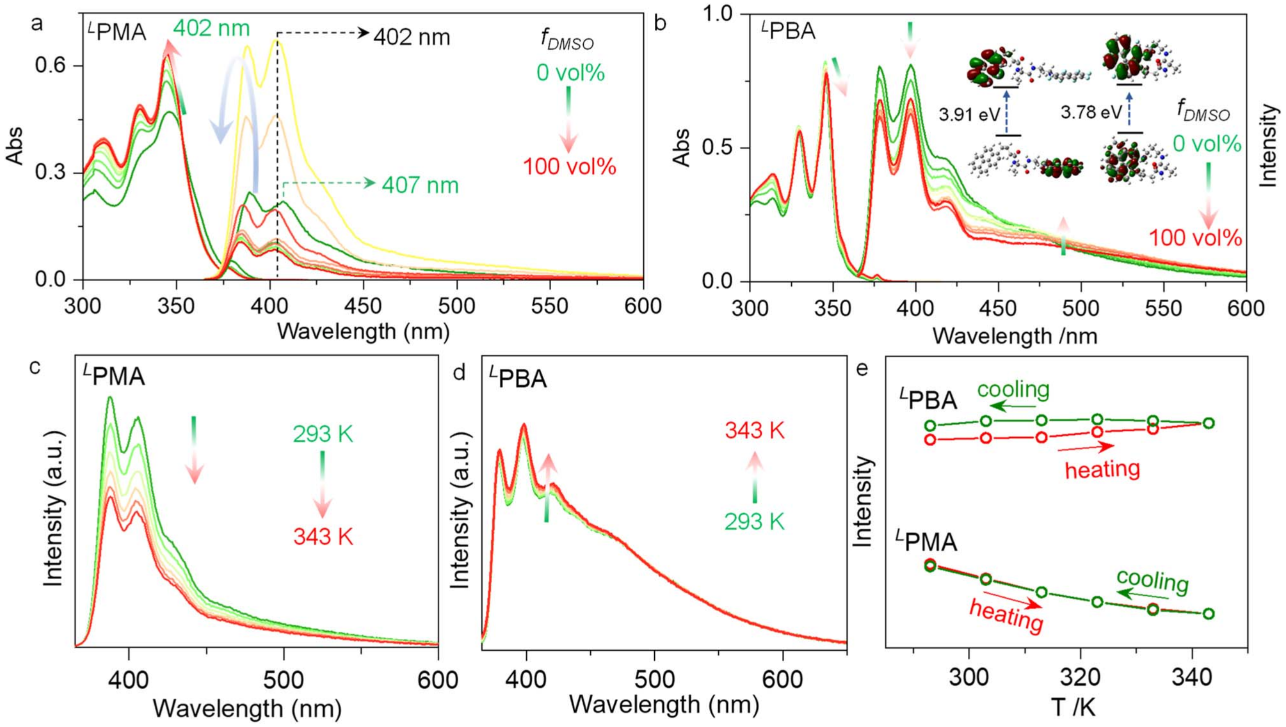

Fig. 3 (a) Absorption and emission spectra of **^{L}PMA** (0.2 mM) with different volume fractions of DMSO (f_{DMSO}) against CHCl$_3$. (b) Absorption and emission spectra of **^{L}PBA** (0.2 mM) with different volume fractions of DMSO (f_{DMSO}) against CHCl$_3$. The inset shows the HOMO–LUMO gap of the free monomer and folded **^{L}PBA**. Temperature-variable emission spectra of (c) **^{L}PMA** and (d) **^{L}PBA** in DCE (0.2 mM), as well as (e) the summarized max. intensity as a function of temperature.

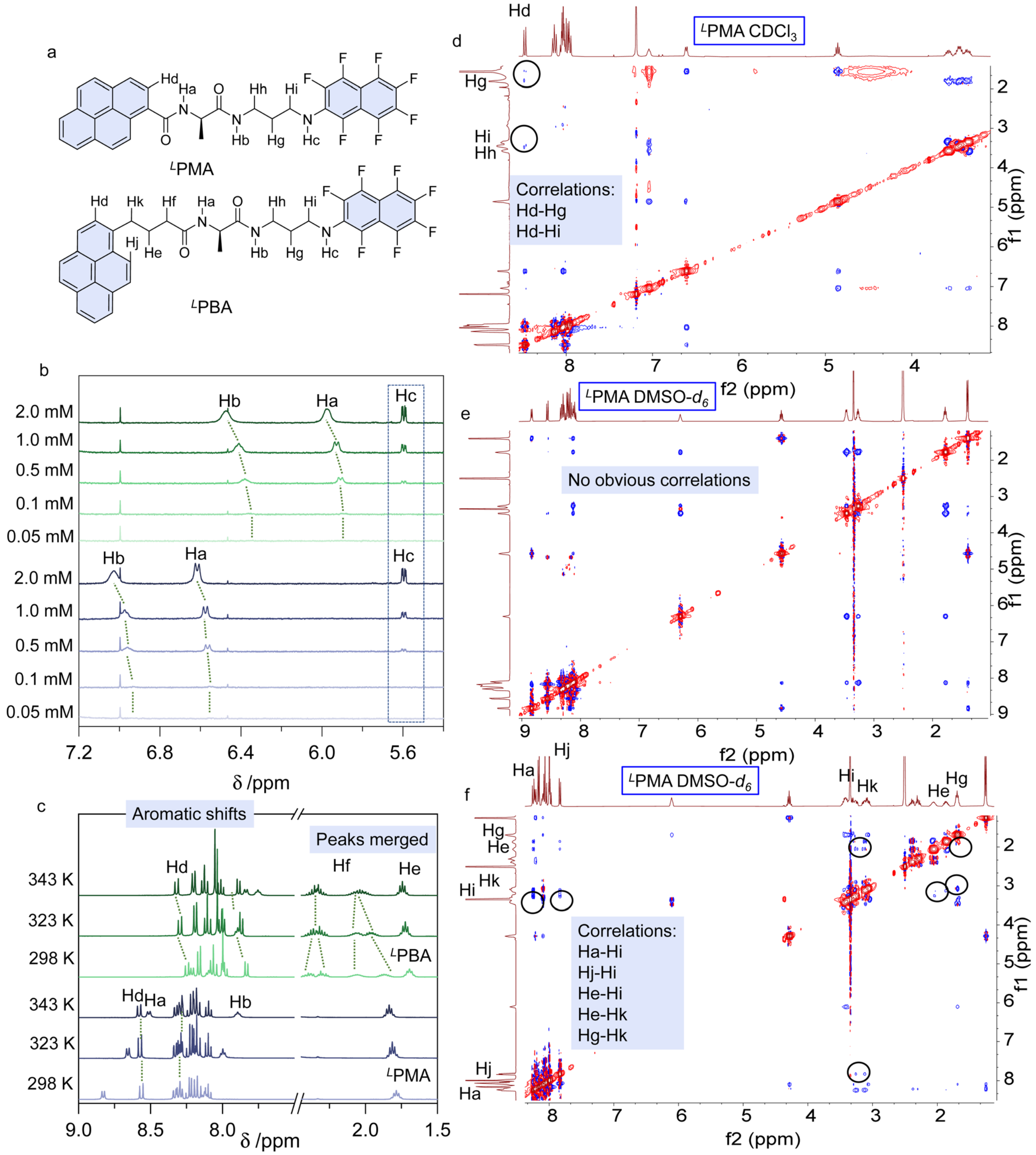

Fig. 4 ^{1}H NMR studies. (a) Proton assignments of ^{L}PMA and ^{L}PBA. (b) Concentration-dependent ^{1}H NMR spectra of ^{L}PMA and ^{L}PBA in $CDCl_3$. (c) Temperature-variable ^{1}H NMR spectra of ^{L}PMA and ^{L}PBA in DMSO-d_6 (10 mM). (d–f) 2D NOESY spectra of ^{L}PMA and ^{L}PBA in $CDCl_3$ (saturated) and DMSO-d_6 (10 mM).

He of the alkyl spacers at low temperatures are split, caused by the chiral conformations, which are merged upon heating. These changes are possibly due to the transformation from a folded to unfolded structure. Two-dimensional (2D) nuclear Overhauser effect spectroscopy (NOESY) is a powerful tool for precise assignment of protons and proton–proton correlations. For **^{L}PMA**, we found correlations including Hd–Hg and Hd–Hi in $CDCl_3$. The long distances between the protons evidence the formation of dimers with structures similar to those in the solid phase X-ray analysis (Fig. 4d). However, in DMSO-d_6 (c = 10 mM), no proton correlations were found, disregarding the protons with intrinsic close contact (Fig. 4e). Therefore, it is confirmed that **^{L}PMA** adopts dimers and free monomers in $CHCl_3$ and DMSO, respectively. For **^{L}PBA**, due to the low solubility in $CDCl_3$, the splitting of hydrogen in 2D NOESY is not obvious where Hi/Hh/Hk and He/Hf overlap. However, long distance proton correlations such as Hj–Hi, Hi–Hk and Hg–He/Hf probably exist, in good agreement with the dimerization conformation found in solid structure X-ray analysis (Fig. S45 and S46†). In contrast, in DMSO-d_6, strong proton–proton correlations exist, such as Ha–Hi, Hj–Hi, He–Hi, He–Hk and Hg–Hk. This verifies the formation of foldamers in the dipolar DMSO phase. Based on the 1D and 2D ^{1}H NMR, it can be concluded that $^{\mathrm{L}}$**PBA** gives dimers and foldamers in $CHCl_3$ and DMSO, respectively.

Two-dimensional diffusion ordered NMR spectroscopy (DOSY) is a powerful technique to study molecular geometries in solution. According to the Stokes–Einstein equation, the diffusion coefficient *D* is associated with the hydrodynamic radius, and thus the two-dimensional geometry can be predicted.[47–49] The viscosities of solvents at various temperature were recorded using a fitting curve (Fig. S47 and S48†). DOSY spectra of $^{\mathrm{L}}$**PMA** and $^{\mathrm{L}}$**PBA** in $CDCl_3$ and DMSO-d_6 at different temperatures were collected (Fig. S49–S56†), and the diffusion coefficients as well as the hydrodynamic radii are summarized in Table 1 (Fig. S57–S64†). Using an oblate spheroid model (length b > width a), the size parameters were predicted based on the Stokes–Einstein equation. The r values, defined as the ratios of the hydrodynamic radii of the oblate model to the equivalent radii from the volume of the spheroid, are close to 1.0, indicating the validity of the prediction. The p values calculated using b/a represent the aspect ratio. In $CDCl_3$, upon increasing the temperature from 25 °C to 45 °C, the p value of $^{\mathrm{L}}$**PMA** decreases from 4.2 to 2.3, and $^{\mathrm{L}}$**PBA** decreases from 3.2 to 1.7. The decreased aspect ratio agrees with the disassociation of dimers by heating. In DMSO-d_6, the p value of $^{\mathrm{L}}$**PMA** is not changed by heating. This means that $^{\mathrm{L}}$**PMA** retains a monomeric free state independent of thermovariations. However, the p value of $^{\mathrm{L}}$**PBA** shows a significant increase from 1.7 to 3.0 upon heating. This increasing aspect ratio is consistent with the unfolding of the foldamers, which also verifies the assumption based on the 1D ^{1}H NMR results (Fig. 4).

Based on the above results, a brief summary of the structures in solution are shown in Fig. 5. For PMA, in the low polar solvent ($CHCl_3$), dimeric self-assembly is generated by AP force and hydrogen bonds. Upon replacing $CHCl_3$ with the dipolar solvent DMSO, disassociation and transformation into monomers occur. Heating also breaks down the non-covalent forces, generating monomers in low polarity solvents. PMA failed to afford folded structures due to the rigid skeleton and energy barrier. Elongating alkyl spacers with enhanced structural flexibility result in the possibility of forming folded structures. PBA with enhanced flexibility also features dimerization in $CHCl_3$. At a high temperature in $CHCl_3$, PBA forms foldamers. Switching the solvent to polar DMSO transforms PBA into folded structures. Further heating the DMSO solution would destroy hydrogen bonds and intramolecular AP interaction to afford monomers. The structural evolution provides a rational and precise control strategy for molecular folding and supramolecular complexation.

The building units are intrinsically chiral due to the alanine segments. In $CHCl_3$, $^{\mathrm{L}}$**PMA** and $^{\mathrm{D}}$PMA feature negative and positive signals in the pyrene absorption region (300 to 350 nm), indicating the chirality transfer from alanine segments to pyrene pendants (Fig. 6a). The dimeric form possesses better shape resistance compared to the monomers that afford enhanced chiroptical signals. In DMSO, the monomers show reduced CD signals, agreeing with our speculations (Fig. S65†). The tendency is inverted for PBA (Fig. 6b). The DMSO solution gives more intense CD signals than $CHCl_3$ (Fig. S66†). Based on the NMR studies, PBA in DMSO and $CHCl_3$ preferably adopts folded and dimer

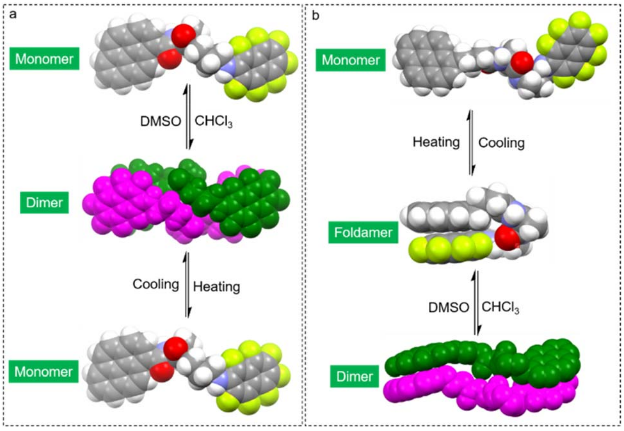

Fig. 5 Space-filling models to demonstrate the structural evolution by solvent and thermal treatments. (a) $^{\mathrm{L}}$PMA, (b) $^{\mathrm{L}}$PBA.

Table 1 Diffusion rates, hydrodynamic radii and other parameters based on DOSY spectra[a]

Entry	T [°C]	D [μm^2 s^{-1}]	Radius [Å]	b [Å]	a [Å]	p	r
$^{\mathrm{L}}$**PMA** ($CDCl_3$)	25	1040	3.9	5.5	1.3	4.2	1.02
	45	1050	4.5	7.0	3.0	2.3	1.02
$^{\mathrm{L}}$**PBA** ($CDCl_3$)	25	691	5.9	8.0	2.5	3.2	1.03
	45	974	4.8	5.7	3.3	1.7	1.00
$^{\mathrm{L}}$**PMA** (DMSO-d_6)	25	161	6.9	8.9	3.0	3.0	0.99
	50	310	6.0	8.5	2.8	3.0	1.08
$^{\mathrm{L}}$**PBA** (DMSO-d_6)	25	157	7.1	8.2	4.9	1.7	0.99
	50	284	6.6	8.7	2.9	3.0	1.01

[a] T and D represent the temperature and diffusion coefficients; b and a are the length and width of the oblate spheroid model, p is the aspect ratio, and r is a parameter close to 1.0 to reflect the reliability.

geometries, respectively. In the foldamer form, the structures are regarded as more rigid due to the clamp topology, and thus enhanced Cotton effects are expected. Next, we evaluated the thermal effects on the chiroptical properties. In DMSO, **^{L}PMA** remains in a monomeric state, and increasing the temperature from 293 K to 358 K barely changes the CD signals. The negative changes agree with the monomer state, which shows no structural variation upon heating–cooling cycling. However, in $CHCl_3$, an increase from 293 K to 328 K results in a CD signal reduction, which can be fully recovered after cooling (Fig. S67†). The phenomenon is consistent with the dimer to monomer structural transformation. **^{L}PBA** exhibited more profound chiroptical changes with the variation of temperature (Fig. 6c, d and S68†). Increasing the temperature of **^{L}PBA** in DMSO from room temperature to 363 K resulted in continuously decreasing Cotton effects. This process is accompanied by the unfolding behavior, and complete recovery occurs during the cooling process without any hysteresis. In DCE (replacing $CHCl_3$ considering the boiling point), a similar propensity was observed.

Spontaneous self-assembly by solvent processing can generate ordered nanoarchitectures. This structural evolution was realized using a nanoprecipitation protocol.[50] By dispersing building units from $CHCl_3$ into MCH, self-assembly was triggered through a good/poor solvent exchange. Before testing, the samples were aged for 12 h. The final concentration of the samples is 1 mM and the volume ratio of $CHCl_3$ and MCH is 2/8. The dispersion of **^{L}PMA** under transmission electron microscopy (TEM) shows planar nanosheets with a rectangular shape, indicating a crystallization-induced aggregation pathway (Fig. 7a). In contrast, **^{L}PBA** generated a nanorod architecture with lengths up to several micrometers and widths of about 200 nm (Fig. 7b). The screw sense and helical nanoarchitectures were not found, possibly because of the dimerization effect that hinders 1D extension to amplify the macroscopic chirality. Atomic force microscopy (AFM) was employed to examine the thickness (Fig. 7c and d). A high aspect ratio was found in the nanosheet morphology of **^{L}PMA**. A thickness of 35 nm was observed from the cross-section profile, indicating its 2D planar nature. Rod structures with thicknesses of about 60 nm were observed in the **^{L}PBA** self-assemblies (Fig. 7d). The CD spectra of the self-assemblies were recorded (Fig. 7e, f and S69†). The spectra are different to those measured in solution phase, due to aggregation introduced asymmetric packing of building units to afford supramolecular chirality, in addition to the chirality in the dimers or foldamers. Additionally, the relatively intense CD signals originate from the more closely packed nanosheets or nanorods, which showed similar peaks to those of the crystalline powder, indicating that the nanostructures have the same molecular packing model (Fig. S70†). Consequently, self-assembly behaves as a valid protocol to manipulate chiroptical properties in addition to the above discussed control methods. The aggregates were collected and subjected to X-ray diffraction (XRD) to explore the molecular arrangements (Fig. 7g). Compared with the simulated powder patterns from X-ray single crystallography, similar patterns were found, suggesting that these nanostructures share similar molecular packing arrays. However, there was clear specific plane selective exposure or growth present in the aggregation thanks to the relative kinetic control of the aggregation. In addition, the experimental XRD of **^{L}PMA** consists of the first and second order diffraction peaks with a distance ratio of $1:1/\sqrt{3}$, and is assigned as hexagonal packing. **^{L}PBA** features a different packing mode, with a distance ratio of $1:1/2:1/3$, which is consistent with a typical lamellar structure. In the X-ray structures of **^{L}PMA** (Fig. 7h), the dimers (intertwined magenta/green structure) in the top view pack into a hexagonal structure, between which hydrogen bonds behave as linkers. This packing is in good agreement with the XRD patterns. For **^{L}PBA**, the dimers pack into layers *via* hydrogen bonds as well, and the layers further pack into lamellar structures, which verifies the observation from the XRD patterns. For the self-assembly of **^{L}PMA** and **^{L}PBA** in a polar solvent environment (DMSO/H_2O), various nanostructures are shown, compared with the aggregations in a nonpolar solvent ($CHCl_3$/MCH). Both **^{L}PMA** and **^{L}PBA** assembled into fused micelles, as shown by the TEM and AFM results, of about 100 nm in diameter, which also showed in dynamic light scattering (DLS) patterns (Fig. S71–S73†). The CD spectra of the self-assemblies are different to those measured in nonpolar environments, due to the fact that the polar solvent could form hydrogen bonds with **^{L}PMA** and **^{L}PBA**, resulting in competition, which does not benefit the growth of 2D and 3D nanostructures. Moreover, the direction and shape of the CD signals were similar to those in the solution phase (Fig. S74†). Thus, the assembled morphology and corresponding chiroptical properties could also be controlled by adjusting the solvent polarity.

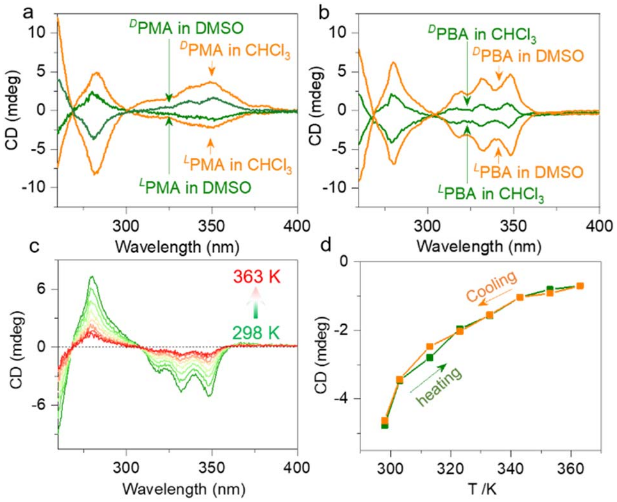

Fig. 6 Chiroptical properties. (a) CD spectra of PMA enantiomers in $CHCl_3$ and DMSO (0.3 mM). (b) CD spectra of PBA enantiomers in $CHCl_3$ and DMSO (0.3 mM). (c) Temperature-variable CD spectra of ^{L}PBA (0.3 mM) in DMSO. (d) CD signal at 350 nm in DMSO of ^{L}PBA (0.3 mM) during heating and cooling cycles.

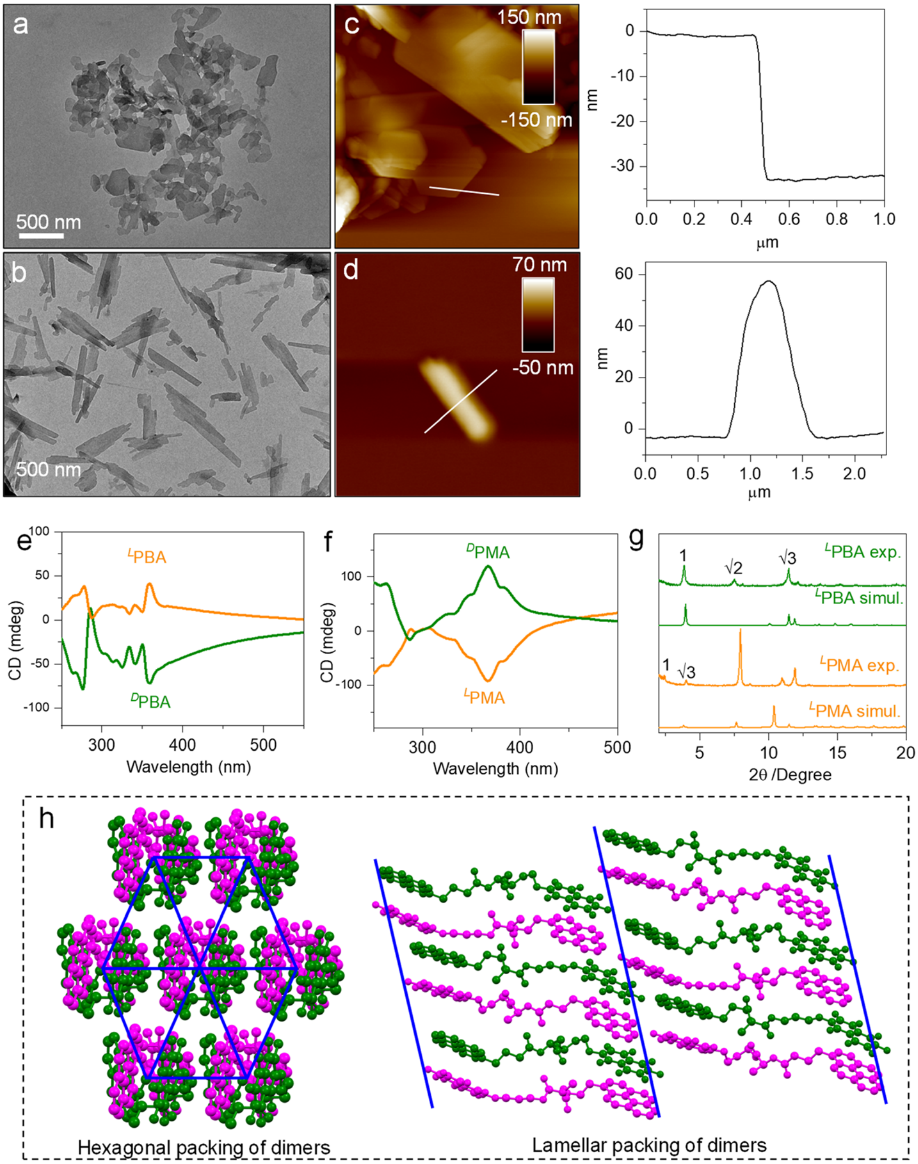

Fig. 7 Self-assemblies. (a and b) TEM images of self-assembled ^{L}PMA and ^{L}PBA in a mixture of $CHCl_3$/MCH (2/8 by volume, 1 mM); (c and d) the corresponding AFM images and cross-section profiles (3 × 3 µm and 5 × 5 µm, respectively); (e and f) CD spectra of self-assemblies. (g) XRD pattern comparison between simulated powder patterns and experimental results; (h) hexagonal and lamellar packing of dimers of ^{L}PMA and ^{L}PBA, respectively.

Conclusions

In this work, amino acid derivatives PMA and PBA bearing pyrene and naphthalene-F_7 segments were designed and synthesized. Using X-ray crystallography, diverse self-assembly modalities were unveiled. PMA self-assembled into double helical dimers in the enantiopure state, while the racemates generated planar achiral dimers. PBA self-assembled into planar dimers in its enantiopure form, while the racemic form gave foldamers. All the folding and dimerized structures featured hydrogen bonding and AP interaction. In the solution phase, we used 1D and 2D ^{1}H NMR to evidence the structural evolution. This demonstrated that the PMA monomer in DMSO is transformed into dimers when the solvent is changed to a less polar solvent such as $CHCl_3$. Additionally, PBA adopts dimer and foldamer structures in $CHCl_3$ and DMSO, respectively. Both of the self-assemblies and foldamers show reversible responses to heating–cooling cycles. By differential self-assembly behavior, PMA and PBA displayed distinct chiroptical activities in response to the solvent polarity. Finally, we showed control of the self-assembly at the nanoscale, and PBA and PMA adopted hexagonal and lamellar packing, respectively. This work introduces a multi-control protocol to tune the preference towards chiral folding and self-assembly at different hierarchical levels, which may facilitate the rational fabrication of functional chiral materials.

Experimental

Materials, experimental details, and additional CD, ^{1}H NMR, and MS spectra can be found in the ESI.†

Data availability

Crystallographic data in CIF format has been deposited with the Cambridge Structural Database. Date supporting this manuscript has been provided in the ESI.†

Author contributions

Q. Cheng carried out the main experiments and data analyzing. P. Xing and A. Hao proposed the assumption and wrote the paper.

Conflicts of interest

There are no conflicts to declare.

Acknowledgements

This work is supported by the National Natural Science Foundation of China (No. 21901145, 22171165) and Natural Science Foundation of Shandong Province (No. ZR2022MB080). We also acknowledge the financial support from Youth Cross-Scientific Innovation Group of Shandong University (2020QNQT003). We thank Prof. Di Sun at Shandong University for assistance with the data collection of X-ray crystal structures.

Notes and references

1 M. Liu, L. Zhang and T. Wang, *Chem. Rev.*, 2015, **115**, 7304–7397.
2 L. E. Mackenzie and P. Stachelek, *Nat. Chem.*, 2021, **13**, 521–522.
3 H. Sakaino, D. J. Broer, S. C. J. Meskers, E. W. Meijer and G. Vantomme, *Angew. Chem., Int. Ed.*, 2022, **61**, e202200.
4 C. Kulkarni, A. K. Mondal, T. K. Das, G. Grinbom, F. Tassinari, F. J. Mathijs, M. E. W. Meijer and R. Naaman, *Adv. Mater.*, 2020, **32**, 1904965.
5 Z. Cao, H. Gao, M. Qiu, W. Jin, S. Deng, K.-Y. Wong and D. Lei, *Adv. Mater.*, 2020, **32**, 1907151.
6 S. Huang, H. Yu and Q. Li, *Adv. Sci.*, 2021, **8**, 2002132.
7 Y. Li, K. Liu, X. Li, Y. Quan and Y. Cheng, *Chem. Commun.*, 2020, **56**, 1117–1120.
8 J. Liu, F. Yuan, X. Ma, D. Y. Auphedeous, C. Zhao, C. Liu, C. Shen and C. Feng, *Angew. Chem., Int. Ed.*, 2018, **57**, 6475–6479.
9 J. L. Greenfield, E. W. Evans, D. D. Nuzzo, M. D. Antonio, R. H. Friend and J. R. Nitschke, *J. Am. Chem. Soc.*, 2018, **140**, 10344–10353.
10 L. Milanesi, J. P. Waltho, C. A. Hunter and M. Volk, *Proc. Natl. Acad. Sci. U. S. A.*, 2012, **109**, 19563–19568.
11 H. Li, L. Kou, L. Liang, B. Li, W. Zhao, X. Yang and B. Wu, *Chem. Sci.*, 2022, **13**, 4915.
12 D. Mondal, M. Ahmad, B. Dey, A. Mondal and P. Talukdar, *Nat. Commun.*, 2022, **13**, 6507.
13 K. R. Strom and J. W. Szostak, *J. Am. Chem. Soc.*, 2022, **144**, 18350–18358.
14 I. Okamoto, M. Nabeta, Y. Hayakawa, N. Morita, T. Takeya, H. Masu, I. Azumaya and O. Tamura, *J. Am. Chem. Soc.*, 2007, **129**, 1892–1893.
15 V. Berl, I. Huc, R. G. Khoury, M. J. Krische and J. M. Lehn, *Nature*, 2000, **407**, 720–723.
16 D. Nuńez-Villanueva, G. Iadevaia, A. E. Stross, M. A. Jinks, J. Swain and C. A. Hunter, *J. Am. Chem. Soc.*, 2017, **139**, 6654–6662.
17 S. Shen, G. V. Baryshnikov, Q. Xie, B. Wu, M. Lv, H. Sun, Z. Li, H. Ågren, J. Chen and L. Zhu, *Chem. Sci.*, 2023, **14**, 970.
18 J. Li, P. Li, M. Fan, X. Zheng, J. Guan and M. Yin, *Angew. Chem., Int. Ed.*, 2022, e202202532.
19 S. Datta and D. Chaudhuri, *Angew. Chem., Int. Ed.*, 2022, e202201956.
20 M. Dharmarwardana, S. Pakhira, R. P. Welch, C. Caicedo-Narvaez, M. A. Luzuriaga, B. S. Arimilli, G. T. McCandless, B. Fahimi, J. L. Mendoza-Cortes and J. J. Gassensmith, *J. Am. Chem. Soc.*, 2021, **143**, 5951–5957.
21 M. Mahl, M. A. Niyas, K. Shoyama and F. Würthner, *Nat. Chem.*, 2022, **14**, 457–462.
22 Z. Wang, A. Hao and P. Xing, *Angew. Chem., Int. Ed.*, 2020, **59**, 11556–11565.
23 Z. Wang, A. Hao and P. Xing, *Chin. Chem. Lett.*, 2021, **32**, 1390–1396.
24 Z. Wang, Y. Li, A. Hao and P. Xing, *Angew. Chem., Int. Ed.*, 2021, **60**, 3138–3314.
25 W. Ji, Y. Tang, P. Makam, Y. Yao, R. Jiao, K. Cai, G. Wei and E. Gazit, *J. Am. Chem. Soc.*, 2021, **143**, 17633–17645.
26 M. Dergham, S. Lin and J. Geng, *Angew. Chem., Int. Ed.*, 2022, **61**, e2021142.
27 J. Kim, J. Lee, W. Y. Kim, H. Kim, S. Lee, H. C. Lee, Y. S. Lee, M. Seo and S. Y. Kim, *Nat. Commun.*, 2015, **6**, 6959.
28 S. Bagatur and T. Fuhrmann-Lieker, *J. Eur. Opt. Soc.: Rapid Publ.*, 2019, **15**, 1530.
29 E. Sánchez-Santos, J. J. Garrido-González, L. F. Rodríguez-Sahagún, A. Habib, Á. L. F. de Arriba, F. Sanz, E. M. M. del Valle, J. R. Morán and V. Alcázar, *Org. Biomol. Chem.*, 2022, **20**, 7972–7980.
30 Z. Wang, H. Ai, A. Hao and P. Xing, *Chem. Mater.*, 2022, **34**, 10162–10171.
31 W. Ji, B. Xue, Y. Yin, S. Guerin, Y. Wang, L. Zhang, Y. Cheng, L. J. W. Shimon, Y. Chen, D. Thompson, R. Yang, Y. Cao, W. Wang, K. Cai and E. Gazit, *J. Am. Chem. Soc.*, 2022, **144**, 18375–18386.
32 J. Xu, Q. Chen, S. Li, J. Shen, P. Keoingthong, L. Zhang, Z. Yin, X. Cai, Z. Chen and W. Tan, *Angew. Chem., Int. Ed.*, 2022, e202202571.
33 E. K. Roesner, D. Asheghali, A. Kirillova, M. J. Strauss, A. M. Evans, M. L. Becker and W. R. Dichtel, *Chem. Sci.*, 2022, **13**, 2475.
34 T. Kim, J. Hong, J. Kim, J. Cho and Y. Kim, *J. Am. Chem. Soc.*, 2023, **145**, 1793–1802.

35 H. Lin, X. Chang, D. Yan, W.-H. Fanga and G. Cui, *Chem. Sci.*, 2017, **8**, 2086.

36 G. Y. Lee, E. Hu, A. L. Rheingold, K. N. Houk and E. M. Sletten, *J. Org. Chem.*, 2021, **86**, 8425–8436.

37 H. Zhang, J. Han, X. Jin and P. Duan, *Angew. Chem., Int. Ed.*, 2021, **60**, 4575–4580.

38 J. Zhao, B. Wang, A. Hao and P. Xing, *Nanoscale*, 2022, **14**, 1779.

39 T. Lu and F. Chen, *J. Comput. Chem.*, 2012, **33**, 580–592.

40 E. R. Johnson, S. Keinan, P. Mori-Sánchez, J. Contreras-García, A. J. Cohen and W. J. Yang, *J. Am. Chem. Soc.*, 2010, **132**, 6498–6506.

41 P. R. Spackman, M. J. Turner, J. J. McKinnon, S. K. Wolf, D. J. Grimwood, D. Jayatilaka and M. A. Spackman, *J. Appl. Crystallogr.*, 2021, **54**, 1006–1011.

42 O. Wallach, *Liebigs Ann. Chem.*, 1895, **286**, 90–143.

43 J. Marciniak, M. Andrzejewski, W. Cai and A. Katrusiak, *J. Phys. Chem. C*, 2014, **118**, 4309–4313.

44 Y. Xu, C. Li, Q. Cao, B. Wang and Y. Xie, *Dyes Pigm.*, 2017, **139**, 681–687.

45 M. Elldrissi, S. J. Teat, P. F.-X. Corvini, M. J. Paterson and S. J. Dalgarno, *Chem. Commun.*, 2017, **53**, 1973–1976.

46 Y. Zhang, B. He, J. Liu, S. Hu, L. Pan, Z. Zhao and B. Tang, *Phys. Chem. Chem. Phys.*, 2018, **20**, 9922.

47 L. Avram and Y. Cohen, *Chem. Soc. Rev.*, 2015, **44**, 586–602.

48 Z. Zhang, H. Wang, X. Wang, Y. Li, B. Song, O. Bolarinwa, R. A. Reese, T. Zhang, X. Wang, J. Cai, B. Xu, M. Wang, C. Liu, H.-B. Yang and X. Li, *J. Am. Chem. Soc.*, 2017, **139**, 8174–8185.

49 N. Giuseppone, J.-L. Schmitt, L. Allouche and J.-M. Lehn, *Angew. Chem., Int. Ed.*, 2008, **47**, 2235–2239.

50 S. Bobbala, S. D. Allen and E. A. Scott, *Nanoscale*, 2018, **10**, 5078–5088.